NMR calibration of optical measurement of nuclear polarization in ^{3}He

W. Lorenzon, T. R. Gentile, H. Gao, and R. D. McKeown
W.K. Kellogg Radiation Laboratory, California Institute of Technology, Pasadena, California 91125
(Received 29 June 1992)

We have performed precise NMR measurements in order to calibrate a standard optical technique for measuring the polarization of ^{3}He nuclei. This optical technique requires knowledge of the pressure-dependent relationship between the nuclear polarization and the degree of circular polarization of the 668-nm light emitted from a ^{3}He discharge. We determined the nuclear polarization by comparing the adiabatic fast-passage NMR signal from samples of polarized ^{3}He at pressures between 0.1 and 5 torr to an identical sample of water. For water, the polarization is known from statistical mechanics. The ^{3}He is polarized using the metastability exchange technique for optical pumping of ^{3}He. The accuracy of the calibration is $\pm 2\%$, which is required for applications in nuclear physics.

PACS number(s): 32.80.Bx, 29.29.Pj, 07.60.Fs

I. INTRODUCTION

The developments in the past decade of polarized electron beams and efficient optical pumping of ^{3}He with lasers [1] have renewed interest in nuclear spin-polarized ^{3}He targets for experiments in medium- and high-energy physics. These experiments require accurate measurements of the nuclear polarization of the ^{3}He target. Nuclear magnetic resonance (NMR) techniques can provide direct and accurate measurements of the nuclear polarization, but are not always convenient in accelerator environments. Therefore we have performed precise NMR measurements that calibrate a simple optical technique for measuring the polarization of ^{3}He nuclei. This optical technique, developed by Laloë [2,3], requires knowledge of the pressure-dependent relationship between the nuclear polarization and the degree of circular polarization of the 668-nm light emitted from an electrical discharge in polarized ^{3}He. It is appropriate in the range of pressures where the technique of metastability exchange optical pumping [4] is efficient. Using NMR, we have calibrated this optical technique with an accuracy of $\pm 2\%$ for pressures between 0.1 and 5 torr.

It was nearly 30 years ago that Colegrove, Schearer, and Walters [4] demonstrated the metastability exchange technique for optical pumping of ^{3}He. A constant limitation, however, was the relatively small intensity of the discharge lamps used as optical-pumping sources, which put an upper limit of about 20% on the nuclear polarization. In addition, the pumping rate, i.e., the rate at which ^{3}He atoms can be polarized, was not sufficiently high to balance relaxation mechanisms in targets. In the early 1980's the development of laser sources increased the attainable polarization to 65% and pumping rate to $\sim 10^{17}$ atoms/s. This renewed interest in optical pumping of helium in several fields of physics, including studies of quantum phenomena in the gaseous and fluid phase at low temperatures [5,6], polarization of electrons and ions [7], polarizing thermic and epithermic neutron beams [8], and polarized targets for nuclear physics experiments [9,10]. With the recent development of the arc-lamp-pumped neodymium-doped lanthanum magnesium hexaluminate (Nd:LMA) laser, polarization up to 85% and pumping rates of $10^{18}-10^{19}$ atoms/s have been obtained [11–13]. These improvements in the attainable polarization have motivated more accurate measurements of the polarization for applications and intrinsic interest in the optical-pumping process.

In medium- and high-energy nuclear physics, polarized ^{3}He targets are interesting because the spin-dependent properties of the polarized ^{3}He nucleus are dominated by the neutron in the nucleus. Because the two protons are predominantly in a spin singlet state, the neutron carries most (90%) of the spin of the nucleus [14]. Quasielastic scattering of electrons from polarized ^{3}He yields information about the electric and magnetic form factors of the neutron. This has been demonstrated by a recent experiment by Woodward *et al.* [15]. Experimental programs using polarized beams and polarized ^{3}He targets are planned for all major accelerator laboratories [Bonn, Continuous Electron Beam Accelerator Facility (CEBAF), Deutsches Elektronen-Synchrotron (DESY), Mainz, MIT-Bates, Novosibirsk, and Stanford Linear Accelerator (SLAC)]. To obtain the high target densities required for these experiments, polarized ^{3}He targets have been developed with densities enhanced by either low-temperature techniques [9,16] or by mechanical compression [12,17,18]. (The metastability exchange technique is only efficient at pressures ~ 1 torr.) Alternatively, low-density "internal" targets [9,19] that take advantage of the high effective beam current in storage rings have been developed.

Historically, polarization of ^{3}He nuclei produced by metastability exchange optical pumping has been measured by NMR and two indirect optical methods. In the technique of metastability exchange optical pumping, ^{3}He metastables are produced by a weak electrical discharge and polarized by optical pumping. The nuclei become polarized when the polarization is transferred to the ground-state atoms in metastability exchange collisions. One optical method [4], which we refer to as the pump light absorption technique, utilizes the change in

the absorption of light at the optical-pumping wavelength. As the polarization increases, the absorption of the pumping light decreases because the population in the metastable state shifts to magnetic sublevels that do not interact with this light. Hence this method actually measures the metastable polarization, which should be equal to the ground-state polarization due to the close coupling provided by the metastability exchange collisions. In recent years, the accuracy of this technique has been improved by using a probe beam from a narrow-band, stable, diode laser-pumped Nd:LMA laser [20]. However, an accurate measurement is difficult because the absorption for small cells is typically only a few percent.

The second optical method is the subject of our work. (In the remainder of this paper, we refer to this method simply as the "optical technique" because we do not discuss the pump light absorption technique any further.) This method is completely nonperturbative and well suited to long-term, remote applications. In this approach the degree of circular polarization of the 668-nm light emitted by the discharge is monitored, which can be related to the nuclear polarization. However, because this relationship depends on pressure, it must be calibrated against either the pump light absorption technique or NMR measurements. Such a calibration was performed in 1974 by Pinard and Van Der Linde [21] using absorption of the pumping light from a ^{4}He lamp. Because the accuracy of these measurements was not quoted in Ref. [21] and was subject to systematic errors associated with lack of knowledge of the spectrum of the lamp, we have repeated the calibration using NMR. Concurrently with our work, a calibration against the pump light absorption technique using a diode laser-pumped Nd:LMA laser has been performed by Bigelow, Nacher, and Leduc [22]. The results of Bigelow, Nacher, and Leduc are consistent with our data.

To avoid uncertainties associated with an absolute NMR measurement, we have compared our NMR signals from ^{3}He to the signal from an identical water sample. For water the polarization is known from statistical mechanics. The NMR measurements are performed using the technique of adiabatic fast passage. The advantage of this technique is that the line shape of the NMR signal is identical for water and ^{3}He, which facilitates the comparison.

The outline of the paper is as follows. Section II contains a brief description of the theory for the NMR and optical techniques for measuring polarization in ^{3}He. We describe the apparatus in Sec. III and the measurements in Sec. IV. Appendix A is devoted to a discussion of the calibration of the optical polarimeter and Appendix B contains a short derivation of a result used in the discussion of the optical polarimeter.

II. THEORY

In this section, we review the theory of the NMR and optical techniques for measuring polarization in ^{3}He. Although the principles of NMR have been described in great detail in Ref. [23,24], we review the aspects which are relevant for our discussion.

A. Adiabatic fast passage

Adiabatic fast passage (AFP) is a technique to reverse the direction of a macroscopic magnetization with respect to a static magnetic field. To understand this technique, consider the effect of an oscillating rf magnetic field $\mathbf{B}_x = 2B_1\cos(\omega t)\hat{\mathbf{x}}$ applied to a magnetized sample that is immersed in a static magnetic field $B_0\hat{\mathbf{z}}$. It is useful to transform from the laboratory frame $(\hat{\mathbf{x}},\hat{\mathbf{y}},\hat{\mathbf{z}})$ to a frame $(\hat{\mathbf{x}}',\hat{\mathbf{y}}',\hat{\mathbf{z}}'=\hat{\mathbf{z}})$ rotating at the rf frequency ω. In this rotating frame, decomposing B_x into two rotating fields yields one field that is stationary while the other rotates at the frequency 2ω. Under the conditions of our measurements, the latter can be neglected because it is nonresonant. The effective field in the rotating frame is given by

$$\mathbf{B}_e = \left[B_0 - \frac{\omega}{\gamma} \right] \hat{\mathbf{z}}' + B_1 \hat{\mathbf{x}}' \ , \tag{1}$$

where γ is the gyromagnetic ratio ($\gamma_p/2\pi = 4.26$ kHz/G for protons in water and $\gamma_h/2\pi = 3.24$ kHz/G for ^{3}He). If the static field is initially far enough away from ω/γ so that $|B_0 - \omega/\gamma| \gg B_1$, then $\mathbf{B}_e$ and the magnetization $\mathbf{M}$ are oriented nearly along $\hat{\mathbf{z}}'$ in the rotating frame. If the static field is ramped towards resonance ($B_0 = \omega/\gamma$), $\mathbf{B}_e$ rotates away from the $\hat{\mathbf{z}}'$ axis towards the $\hat{\mathbf{x}}'$ axis and carries the magnetization along with it. At resonance, $\mathbf{B}_e = B_1\hat{\mathbf{x}}'$. If the static field is ramped far past resonance, both $\mathbf{B}_e$ and $\mathbf{M}$ will reverse direction. If the sweep rate dB_0/dt is slow enough (adiabatic condition) so that

$$\left| \frac{dB_0}{dt} \right| \ll \gamma B_1^2 \ , \tag{2}$$

then the magnetization follows the effective field. The "fast" condition requires that the effects of relaxation must be negligible during the time of passage through resonance:

$$\frac{1}{B_1} \left| \frac{dB_0}{dt} \right| \gg \frac{1}{T_1}, \frac{1}{T_2} \ , \tag{3}$$

where T_1 and T_2 are the longitudinal and transverse relaxation times, respectively. In our system, transverse relaxation is dominated by dephasing of the individual precessing spins due to gradients in B_0. However, if

$$B_1 \gg \Delta B_0 \ , \tag{4}$$

where ΔB_0 is the inhomogeneity in B_0 across the sample, transverse relaxation due to gradients can be neglected in Eq. (3) [25,26].

As $\mathbf{M}$ slowly reverses direction it is also rapidly precessing in the laboratory frame at the rf frequency ω. For a pickup coil in the xz plane, this precessing magnetization induces an ac voltage of amplitude $\mathcal{E}$, given by

$$\mathcal{E} = -NQ\frac{d\Phi}{dt} = -NQ\omega\Phi \ , \tag{5}$$

where Φ is the magnetic flux through the pickup coil with N turns and Q is the quality factor of the tuned

pickup circuit. The AFP line shape is

$$\mathcal{E}(B_0)=\mathcal{E}_0\frac{B_1}{[B_1^2+(B_0-\omega/\gamma)^2]^{1/2}}\ , \tag{6}$$

where $\mathcal{E}_0$ is the amplitude of the induced voltage at resonance. The line shape is the same for ^{3}He and water.

For identical samples of ^{3}He and water, all geometrical contributions to the flux would cancel out when evaluating the ratio of the flux from the ^{3}He sample to the flux from the water sample. To account for small differences ($\pm 2\%$) in the volumes of our cells, we corrected the measured values of $\mathcal{E}_0$ to the exact volume of each cell. The ratio R of $\mathcal{E}_0$ obtained from the ^{3}He sample ($\mathcal{E}_0^h$) to that obtained from water ($\mathcal{E}_0^p$) is then given by

$$R=\frac{\mathcal{E}_0^h}{\mathcal{E}_0^p}=\frac{(Q\omega P_n n V\mu)_h}{(Q\omega P_n n V\mu)_p}\ , \tag{7}$$

where P_n is the nuclear polarization, n is the number density of spin-$\frac{1}{2}$ particles with magnetic moment μ, and V is the volume of the cell. The quantities in Eq. (7) have subscripts h and p that denote ^{3}He and water (protons), respectively. P_n is defined by

$$P_n=\frac{n_+-n_-}{n_++n_-}\ , \tag{8}$$

where n_+ and n_- are the number densities for the two eigenstates of the spin with respect to the $\hat{\mathbf{z}}$ axis. The polarization of the protons in water is given by $P_n^p=\tanh(\mu_p\omega_p/kT_p\gamma_p)$, which for our conditions can be accurately approximated by

$$P_n^p=\frac{\mu_p\omega_p}{kT_p\gamma_p}\ , \tag{9}$$

where μ_p is the proton magnetic moment in water, k is the Boltzmann constant, and T_p is the temperature of the water cell at the time of the NMR measurement. The ^{3}He density can be expressed in terms of the pressure p_h and temperature T_h of the ^{3}He cell at the time the cell is sealed off. Finally, if we rearrange Eq. (7) to express P_n^h in terms of known constants and measured quantities, we obtain

$$P_n^h=\frac{(QV\omega^2\mu^2)_p}{(QV\omega\mu)_h}\frac{n_pT_h}{\gamma_pT_pp_h}\ . \tag{10}$$

As with the cell volumes, we have included ω and Q in Eq. (10) to account for small differences between cells (see Sec. III B).

B. Free induction decay

Although the method of adiabatic fast passage is most suitable for these measurements, additional information about the system can be obtained from the technique of free induction decay (FID). In this technique, the static field is fixed and a rf pulse is applied to the sample at the Larmor frequency. In this case, $\mathbf{B}_e=B_1\hat{\mathbf{x}}'$, hence the magnetization precesses around the $\hat{\mathbf{x}}'$ axis at the angular frequency γB_1. If such a rf field is applied for a short time τ, the magnetization vector rotates by an angle $\gamma B_1\tau$. By measuring the pulse length required to rotate the magnetization by $\pi/2$, B_1 was determined. For ^{3}He such a rotation was easy to observe using the optical signal because the nuclear polarization along the $\hat{\mathbf{z}}'$ axis drops to zero. FID was used to confirm that the width of the AFP signal was indeed given by B_1 [see Eq. (6)].

After the pulse the magnetization precesses freely, and decays due to inhomogeneity in B_0. For the water signal, the temporal behavior of the decay is given by the Fourier transform of the spectral distribution of Larmor frequencies. The time scale of the decay is roughly $(\gamma_p\Delta B_0)^{-1}$, i.e., the time required for a spread of 1 rad in the distribution of accumulated phase of the Larmor precession of the individual spins. Measurement of the time scale of the decay allowed estimation of ΔB_0, which was used to check whether Eq. (4) was satisfied. The decay of the ^{3}He signal is much longer than the water signal because each ^{3}He atom experiences the average value of B_0 because of its motion, usually referred to as motional narrowing [27]. Motional narrowing leads to a decay of the transverse magnetization with the simple form $\mathcal{E}(t)=\mathcal{E}_0\exp(-t/\tau)$. The decay time τ increases for longer mean free path, hence it is longer for lower pressure. For helium we observed exponential decays with time constants of 0.35–1.5 s in the range 2.0–0.3 torr.

C. Optical measurement of polarization

The optical method relies on the mixing of polarization from the nucleus to excited electrons via the hyperfine interaction. When ^{3}He atoms are excited to the $3\,^1D_2$ level by electron impact in the discharge, the nuclear spin is unperturbed. During the 15-ns lifetime of the $3\,^1D_2$ state, the nuclear polarization is mixed into electronic polarization by the hyperfine interaction. As a result of this mixing, the subsequent spontaneous emission down to the $2\,^1P_1$ level shows some degree of circular polarization which can be related to the nuclear polarization. However, some of the electronic polarization is lost due to collisions, hence this relationship depends on pressure.

The theory of the pressure dependence of the degree of circular polarization of the 668-nm light has been investigated by Pinard and Van Der Linde [21]. Since we use their results to fit our data, we summarize their work, but refer the reader to Refs. [21,28] for the full details. Let us define P to be the degree of circular polarization of the 668-nm light emitted by the discharge and P_n to be the nuclear polarization. For a $J=2\rightarrow J=1$ transition they obtain

$$\frac{P}{P_n}=\frac{3a^2(\Gamma+\gamma_2)/2}{(\Gamma+\gamma_2)(\Gamma+\gamma_1)^2+6a^2(\Gamma+\gamma_1)(\Gamma+2\gamma_2/3)/\Gamma+a^2(\Gamma-\gamma_1+2\gamma_2)/4}\ , \tag{11}$$

where Γ is the spontaneous emission rate for the transition, and γ_1 and γ_2 are the disorientation and disalignment rates, respectively. The constant a is defined by the hyperfine Hamiltonian, $a\hbar\mathbf{I}\cdot\mathbf{J}$, where $\mathbf{I}$ is the nuclear spin angular momentum and $\mathbf{J}$ is the total electronic angular momentum. For $J=2$, the hyperfine splitting in frequency is $\Omega=5a/2$. The rates γ_1 and γ_2 are related to the corresponding cross sections, σ_1 and σ_2, by $\gamma_i=n\sigma_i v_r$, where n is the density of ground-state atoms and v_r is the mean relative velocity of the two colliding atoms. In addition, to account for other types of collisions that effectively destroy the $3\,^1D_2$ state, Γ is replaced by $\Gamma'=\Gamma+n\sigma_0 v_r$, where σ_0 is the total cross section for these processes. (Note that this cross section is labeled $\sigma_0+\sigma_e$ in Ref. [21].) The three cross sections σ_1, σ_2, and σ_0 are adjusted to reproduce the measured variation of P/P_n with pressure.

In the limit of zero pressure, $\gamma_1=\gamma_2=0$ and Eq. (11) reduces to

$$\frac{P}{P_n}=\frac{0.24}{1+\Gamma^2/\Omega^2}\ . \tag{12}$$

For the $3\,^1D_2$ level, $\Gamma=6.58\times10^7\ \mathrm{s}^{-1}$ [29] and $\Omega=8.74\times10^8\ \mathrm{s}^{-1}$ [30], yielding $P/P_n=0.239$ at zero pressure. However, Pinard and Van Der Linde found that the observed pressure dependence of P/P_n for the $3\,^1D_2$ level was inconsistent with a limit of 0.239 at zero pressure. They speculated that the discrepancy could be due to cascading effects from higher ^1F states that would be manifested as an overall multiplicative correction to P/P_n for data above some critical pressure. Based on this idea, they found that they could fit their data above 0.15 torr if they introduced a normalization parameter Z into Eq. (11). We have also found that this approach is necessary to fit our data. Because we have not observed any dependence of P/P_n on discharge conditions (see Sec. III C 2), we believe that the value of the normalization parameter is related to the physics that governs the pressure dependence of P/P_n, rather than an artifact of any given apparatus.

III. APPARATUS

A. NMR system

The NMR system is shown in Fig. 1. A cylindrical Pyrex cell, 5.0 cm diameter by 5.7 cm long, filled with ^{3}He or water is placed in a homogeneous static magnetic field $B_0\hat{\mathbf{z}}$ that is produced by a pair of 30-cm-radius Helmholtz coils. The rf magnetic field $\mathbf{B}_x$ is generated by the drive coils, a pair of 14.8-cm-radius Helmholtz coils. Two rectangular pickup coils separated by 5.6 cm surround the cell, with their axes in the $\hat{\mathbf{y}}$ direction. Each pickup coil is 6.9 cm long by 6.2 cm wide and has 400 turns.

Obtaining an accurate measurement of the small signal from water (see Sec. IV A) and from low-pressure ^{3}He cells ($\lesssim$0.2 torr) required minimizing noise from vibrations and electromagnetic fields. To shield out electromagnetic fields, the entire system is surrounded by an aluminum box with a wall thickness of 1.6 mm. To minimize mechanical vibrations, the aluminum box is supported by a set of shock absorbers, styrofoam, and springs.

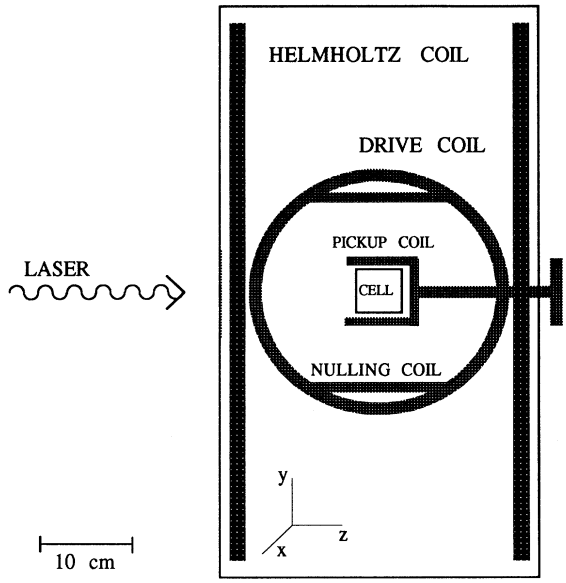

FIG. 1. Scale diagram of the NMR apparatus.

The ^{3}He gas was polarized by optical pumping with an arc-lamp-pumped Nd:LMA laser. The aluminum box has a 9-cm-diameter opening in the front to allow the laser beam to enter and the 668-nm light to exit. The laser light propagates along the $\hat{\mathbf{z}}$ axis; the optical polarimeter is located 6° off the $\hat{\mathbf{z}}$ axis in the xz plane, 95 cm from the cell. A rf high voltage (0.1–20 MHz) applied to two aluminum foil loops taped on the outside of the cell generated a weak electrical discharge in the helium gas. When the cell was in place, the aluminum foil strips made contact with metal electrodes in the pickup coil support. Because the discharge produces substantial rf interference, it is turned off during NMR measurements. With the discharge off, the relaxation of the polarization during the time required for the measurement is less than 0.2%. In addition, it was necessary to ground the amplifier (see Fig. 2) whenever the discharge was on in order to avoid overloading it.

A block diagram of the NMR electronics is shown in Fig. 2. A function generator, tuned to the resonant frequency ($\omega/2\pi=96$ kHz) of the pickup coil system, produces a rf current in the drive coil. The magnetic field B_0 is ramped in 1 s from 2 G below to 2 G above the atomic resonance condition ($\omega/\gamma_h=29.6$ G or $\omega/\gamma_p=22.5$ G). The current in the Helmholtz coil is converted into voltage, digitized, and stored in the computer. This ramp information was used for summing up several sweeps for the water sample (see Sec. IV A). The voltage induced in the pickup coil is amplified by a factor of 100 and then sent to a lock-in amplifier. The two outputs, one in phase with the reference signal and the other in quadrature, are squared and summed before they are digitized and stored in the computer.

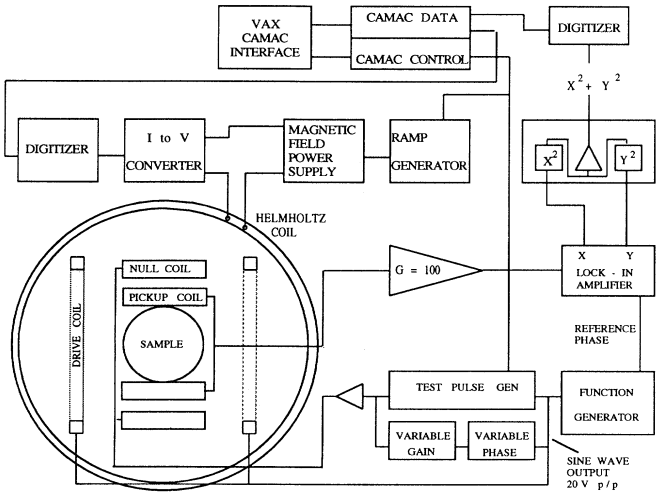

FIG. 2. Block diagram of the NMR electronics.

To minimize cross talk between the drive and the pickup coils, the pickup coil must be normal to the drive coil. As shown in Fig. 1, the pickup coil was mounted such that it could be rotated around the $\hat{z}$ axis from outside the aluminum box. The residual signal in the pickup coil was nulled by applying a gain and phase shifted voltage to the nulling coil. In addition, we determined the quality factor Q of the pickup coil circuit by sweeping the frequency of the nulling coil voltage from 60–120 kHz and measuring the linewidth of the response of the pickup coil. The typical measured value of Q was 60, with variations of $\pm 5\%$ from cell to cell, and $\pm 0.7\%$ for the measurements on a given cell. The Q and resonant frequency of the pickup coil were measured on each day that we acquired data. The resonant frequency varied by $\pm 0.2\%$ from cell to cell.

A test pulse, which is a sine wave packet with a variable width between 0.5 and 20 ms, was used to check the performance of the electronics. Since the signal for water and ^{3}He differ by as much as a factor of 70, the linearity of the electronics is important. Using the test pulse we found the electronics to be linear to within $\pm 1\%$.

B. Cell preparation

We prepared each ^{3}He cell according to techniques that are described elsewhere [4]. Briefly, each cell was evacuated to below 10^{-7} torr, baked overnight at 400 °C, and further cleaned with a strong discharge. Before mounting on the vacuum system, we measured the cell volume with an uncertainty of $\pm 0.2\%$ by filling the cell with alcohol. The cell volumes are nominally 90 cm^3, with variations of $\pm 2\%$ from cell to cell. The cells were filled with 99.995% pure ^{3}He.

When a cell was sealed off, we measured the pressure in the vacuum manifold, p_h, and the ambient temperature T_h. For pressures below (above) 1 torr, the pressure was measured using a MKS Instruments, Inc. Model 390 (122A) capacitance manometer with a quoted accuracy of $\pm 0.08\%$ ($\pm 0.5\%$). However, we found an additional systematic error rooted in an observed difference between the pressure in the vacuum manifold and the actual pressure in the cell. This difference was measured in the following test: We constructed a "test cell" that had an additional connection to a second capacitance manometer. The volume of the capacitance manometer and connecting tubing was much smaller than the cell volume, so this arrangement simulates the conditions under which our standard cells were constructed. We found that the cell pressure drops as soon as the connection to the vacuum manifold is heated. (If the glass is not melted, this pressure drop is reversible.) The origin of this pressure gradient is not understood. After sealing off the cell and allowing the system to cool, the cell pressure was lower than the original pressure and the remaining pressure in the manifold was higher. Since atoms are conserved, the pressure in the vacuum manifold increases by an amount that depends on the relative volume of the manifold and the cell. The test cell was sealed off and reattached several times and the decrease in the cell pressure measured to be $2.8 \pm 1.5\%$. Unfortunately, this effect was not discovered until all of our cells had been filled and measurements completed. In order to be certain that we had not introduced any systematic errors in the pressure measurement, we refilled nearly all of our cells using an improved technique. We installed a valve very close to the location at which the cell is sealed off. Before sealing the cell, the valve is closed, yielding a manifold volume of about 1.5% of the cell volume. In this configuration, when a test cell was sealed off as described above, the cell pressure after sealing was within 0.3% of the original manifold pressure. All cells except those at 3 and 5 torr were refilled with this procedure. For pressures of 0.8, 1.0, and 2.0 torr, the comparison of data acquired from cells filled with this procedure versus the original procedure was consistent with the measured drop of the test cell pressure of $2.8 \pm 1.5\%$ in the original procedure. Based on these results, the measured decrease of 2.8% was applied to the data acquired on the cells at 3 and 5 torr. Below 0.5 torr, the comparison was not consistent with the expected 2.8% drop, but rather implied that the pressure had dropped by 7% when filled with the original procedure. The reason for this discrepancy is not understood, but we note that we did not do test cell measurements at all pressures. In conclusion, all of our data except at 3 and 5 torr were acquired using the filling procedure with a small vacuum manifold, where we estimate the uncertainty in the cell pressure to be $\pm 0.5\%$. For the cells at 3 and 5 torr, there is a $2.8 \pm 1.5\%$ correction associated with the filling procedure.

Finally, there is another effect on the pressure that we believe is worth noting. We observed a tendency of the NMR signal to drop by as much as 10% at 0.3 torr if the electrical discharge was left on for many hours. However, if the discharge was extinguished, the NMR signal would increase after many hours with the discharge off. Although we cannot present conclusive data, we believe that helium atoms can be temporarily driven into the cell walls, thereby lowering the pressure. We were careful to not leave the discharge on for long periods of time.

C. Optical polarimetry

The polarimeter used to measured the degree of circular polarization of the 668-nm light emitted from the discharge is shown in Fig. 3. Although this system has been described in Refs. [2,3], we review the design to facilitate our analysis of its calibration. Circularly polarized 668-nm light from the discharge is converted to linearly polarized light by the rotating quarter-wave plate (R) at the entrance of the polarimeter. The direction of the linear polarization follows the rotating optic axis of the quarter-wave plate. After the analyzing linear polarizer (A), the light intensity oscillates at the frequency 2ω, where ω is the angular rotation frequency of the quarter-wave plate. The amplitude of the oscillation is proportional to the degree of circular polarization of the light. The interference filter (F) allows light whose wavelength lies in a 10-nm band width centered at 668 nm to reach the photomultiplier tube (PMT). The PMT signal is sent to both a lock-in amplifier and a dc amplifier, whose outputs are proportional to the ac and dc components of the signal, respectively. Both signals are then digitized and sent to the computer.

The measured degree of circular polarization of the light is given by

$$P_m = K\frac{A - A_0}{D} , \tag{13}$$

where A and D are the outputs of the lock-in and dc amplifiers, respectively, A_0 is the residual lock-in output when the polarization of the sample is zero (see Sec. IV B) and K is a calibration factor that mainly takes account of the different amplification factors. P_m is reduced slightly because of the static magnetic field (see Sec. III C 3) and the small angle θ between the line of observation and the $\hat{\mathbf{z}}$ axis. The degree of circular polarization, corrected to zero magnetic field and observation along the $\hat{\mathbf{z}}$ axis, is given by

$$P = \frac{M(B_0)}{\cos\theta} P_m , \tag{14}$$

where $M(B_0)$ is the correction related to the static magnetic field. The factor of $\cos\theta$ is derived in Appendix B.

The polarization of the light can be affected by reflections from material near the cell. To minimize such reflections, we covered the back and sides of the cell with black tape so that light emerged only from the front end of the cell and blackened all material near the cell. To avoid excessive heating of the tape, the laser power was limited to 1 W. (Although the highest optical-pumping efficiency would be obtained using a mirror to retroreflect the laser beam back through the cell, we did not use a mirror because it was inconvenient in our system.)

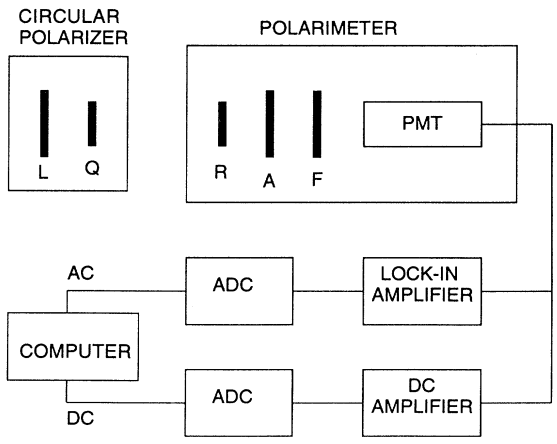

FIG. 3. Schematic diagram of the optical polarimeter. Elements include a rotating quarter-wave plate (R), analyzing linear polarizer (A), 668-nm interference filter (F), photomultiplier tube (PMT), and analog to digital converter (ADC). To calibrate the polarimeter, a circular polarizer constructed from a linear polarizer (L) and a quarter-wave plate (Q) was placed in front of the polarimeter.

1. Calibration

As shown in Fig. 3, the system was calibrated by placing a circular polarizer for 668 nm directly in front of the polarimeter. However, it is important to understand the effect of imperfections in both the circular polarizer and the rotating quarter-wave plate, especially the former. Here we summarize the results of the quantitative analysis presented in Appendix A. Consider a circular polarizer constructed from a linear polarizer (L) followed by a quarter-wave plate (Q). If the retardation of the quarter-wave plate is not exactly $\pi/2$, the emerging light will be elliptically polarized. As one might expect, the signal from the polarimeter depends on the relative orientation of the ellipse with respect to the axis of the analyzing linear polarizer (A). For 99.0% circularly polarized light, the degree of circular polarization registered by the polarimeter varies by $\pm 7.0\%$ as the circular polarizer is rotated around the propagation direction of the light. The true degree of circular polarization of the elliptically polarized light is only obtained when the angle between the analyzing linear polarizer (A) and the ellipse axes is $\pi/4$. To avoid calibration errors, one must use this orientation for the circular polarizer, especially if the quarter-wave plate in the circular polarizer is not of high quality. To obtain an accurate calibration, we use both a high-quality quarter-wave plate and the proper orientation. We observe a variation in the degree of circular polarization registered by the polarimeter of only $\pm 0.6\%$ as the circular polarizer is rotated and by using the proper orientation, the uncertainty in the calibration due to imperfections in the optical elements is negligible. (As shown in Appendix A, the effect of imperfect retardation of the rotating quarter-wave plate is much less critical and can be included in K).

2. Systematics of the optical signal

Since discharge intensity and frequency have a strong effect on the optical pumping of ^{3}He [11], we checked for a possible dependence of P/P_n on discharge characteristics. We did not observe any dependence on either the discharge frequency or intensity. Specifically, the depen-

dence on discharge frequency was tested at pressures of 0.3 and 0.8 torr for discharge frequencies of 0.1, 1.5, and 20 MHz. The test of discharge intensity was performed at 2 torr for a change in the intensity of the light emitted by the discharge of a factor of 5.

As discussed in Sec. III C 1, elliptical polarization of the 668-nm light can lead to an incorrect evaluation of the degree of circular polarization of the light. To test for ellipticity that might result from interaction of the light with the Pyrex cell, we checked for a dependence of P_m on the orientation of the linear polarizer in the polarimeter. This was accomplished by rotating the entire polarimeter about the direction of the incoming light. No dependence was observed within an uncertainty of $\pm 0.5\%$.

In these measurements the angle between the line of observation and the $\hat{z}$ axis, θ, was 6°. In principle, the factor of $\cos\theta$ in Eq. (14) would allow comparison to results obtained at other angles. However, we have seen deviations from the expected $\cos\theta$ dependence at pressures above about 2 torr. As an example, at 2 torr the value of P_m obtained at $\theta = 25°$ was about 10% lower than would be predicted by the $\cos\theta$ rule. The origin of these deviations is not well understood. They may be associated with a combination of depolarization from reflections at the inside of the cell and the nonuniformities that exist in the discharge above about 2 torr. Aside from the pressure, no systematic dependences were found. The deviations observed were typically about the same magnitude as $\cos\theta$ itself. For a small angle of observation such as was used in this experiment, the magnitude of the deviation is smaller than the uncertainties in our measurements. However, if a large observation angle is used, measurements should be cross-calibrated to data taken at small angles.

3. *Magnetic field dependence of optical signal*

The measured degree of circular polarization of the 668-nm light, P_m, decreases with increasing magnetic field because of decoupling of the electronic and nuclear spins. The dependence of P_m on the magnetic field has been calculated [3], but only for the limit of zero pressure. To determine the correction to zero magnetic field, $M(B_0)$, for finite pressure, we measured this dependence at 0.3, 0.8, and 5.0 torr. Because the magnetic field affects the discharge conditions and hence the attainable polarization, we polarized the helium gas at a constant magnetic field of 12 G, changed the magnetic field with the discharge off, and then turned on the discharge to measure P_m at the new value of the field. The calculated results for zero pressure and our measurements are shown in Fig. 4. (P_m has been normalized to 12 G in this graph because of the measurement technique described above.) The observed effect of finite pressure is to weaken the dependence on the magnetic field. For our operating magnetic field, the correction to zero magnetic field is $M(29.6\text{ G}) = 1.017 \pm 0.005$. Although at high magnetic field a pressure dependence is clearly visible in Fig. 4, we used the same correction for all pressures because our measurements were not sufficiently accurate to extract the pressure dependence at 29.6 G.

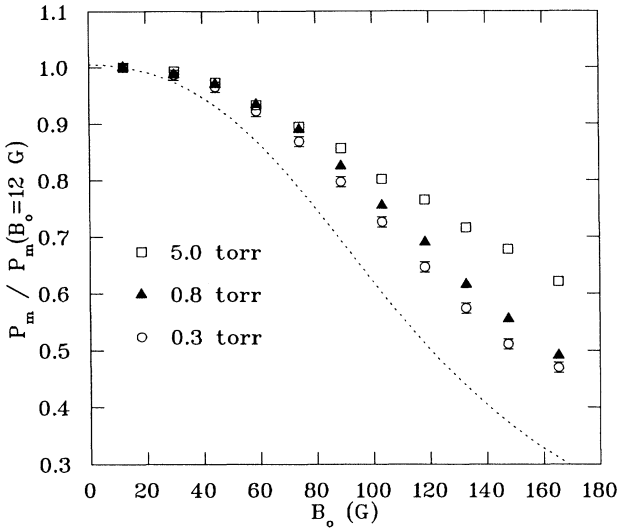

FIG. 4. The measured degree of circular polarization of the 668-nm light, P_m, as a function of the static magnetic field B_0. For each pressure the data have been normalized to the value of P_m obtained at 12 G. Error bars that are not visible are smaller than the size of the points. The dotted line shows the results of a calculation for zero pressure from Ref. [3].

IV. MEASUREMENTS

We begin our discussion of the measurements with the numerical values for the conditions in Eqs. (2)–(4). Using the technique of free induction decay (Sec. II B), we measured B_1 to be 35 ± 1 mG. Hence the sweep rate dB_0/dt of 4 G/s is about 7 times smaller than γB_1^2. T_1 and T_2 are both 3.6 s for water [31], so $1/T_1$ and $1/T_2$ are both 400 times smaller than $(dB_0/dt)/B_1$. For ^{3}He T_1 is typically a few thousand seconds. The inhomogeneity in B_0 across the sample, ΔB_0, was determined to be 1 mG from the observed 30-ms decay time of the FID signal for water. Hence ΔB_0 is about 35 times smaller than B_1.

As described in Sec. III A, we recorded $\mathcal{E}_0^2$, hence we fit the data to the square of Eq. (6), which is a Lorentzian. To establish the magnitude of the noise background, we fit over a range 40 times the full width of the Lorentzian. The observed average half width at half maximum of the Lorentzian line shapes was 36 ± 1 mG, which agrees well with the value obtained from FID. We now describe the measurement procedures for water and ^{3}He, which differ in some respects.

A. Calibration with water

At room temperature and $B_0 = 22.5$ G, the polarization of the protons in the water sample [Eq. (9)] is only $P_p = 7.6 \times 10^{-9}$. The induced voltage $\mathcal{E}_0$ is 130 μV, which after amplification leads to 9-mV rms detected by the lock-in amplifier. To extract the polarization from the induced signal, we must consider the effect of the

3.6-s longitudinal relaxation time on the signal height. Because the sweep time is only 1 s, the polarization at the time of passage through resonance is close to the value at the beginning of the sweep. Hence the signal height depends on whether we ramp from below or from above resonance. We swept symmetrically about the resonance so that the signal height corresponding to the polarization at resonance was obtained by averaging the signal heights from the two sweeps. There is a slight uncertainty of $\pm 0.3\%$ in this averaging procedure due to nonlinearity in the ramp. We also waited 20 s between sweeps to guarantee equilibrium conditions.

To improve the signal-to-noise ratio of the water signal, we averaged the data for ten sweeps (five up and five down). Due to small shifts in the starting time of the ramp (≤ 2 ms), the averaging was done by first correcting the position of the peak for every sweep before adding them up. Figure 5 shows the adiabatic fast-passage signal for water, along with a Lorentzian fit to the data.

Although our technique is based on the idea of comparing NMR signals of ^{3}He and water, we performed a simple calculation to check the magnitude of the observed NMR signal. To evaluate the signal from the water sample, we integrated the contributions to the induced signal from a magnetization distributed uniformly throughout the cell and found that the measured and calculated signal heights agreed within 20%.

B. Measurements with ^{3}He

Since the ^{3}He sample is polarized by optical pumping, the signal height is independent of the initial value of the static field. Figure 6 shows the adiabatic fast-passage signal for a 64% polarized, 1.0-torr cell of ^{3}He.

We measured the calibration factor K and the residual ac signal A_0 each day that data were acquired. Typical day to day variations in K were $\pm 0.5\%$. The residual ac signal A_0 was typically 0–3 % of the optical signal from

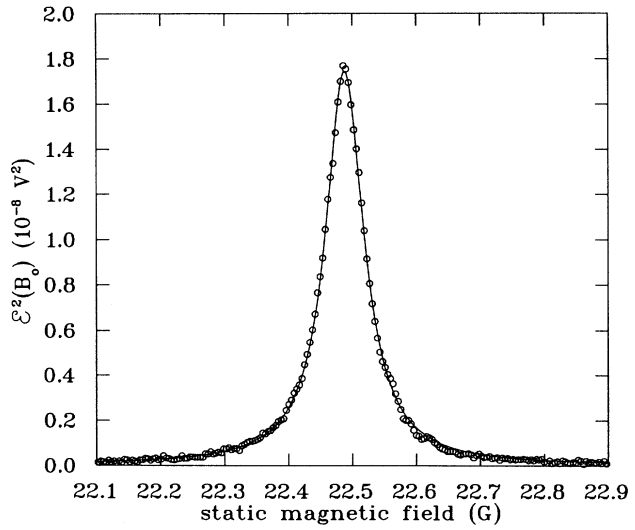

FIG. 5. Adiabatic fast-passage signal for the water cell. The solid curve is a fit to a Lorentzian distribution.

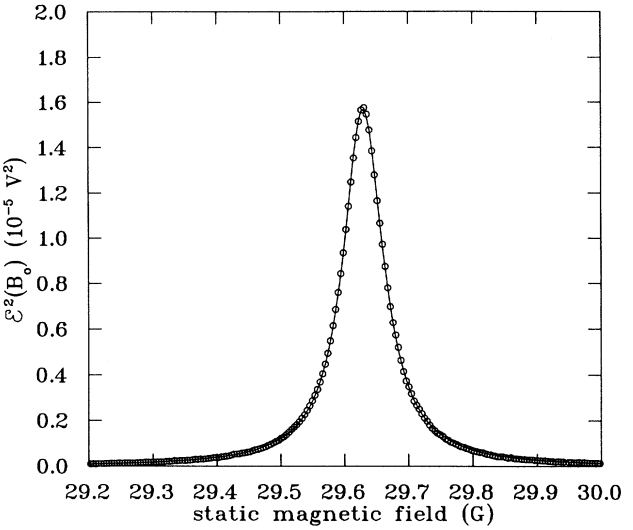

FIG. 6. Adiabatic fast-passage signal for a 1.0-torr cell of ^{3}He ($P_n = 64\%$). The solid curve is a fit to a Lorentzian distribution.

polarized gas. The exact origin of this signal was not determined, although we suspect it was due to electrical noise and/or optical effects of the Pyrex cell. To reduce the statistical uncertainty in the optical measurement to a negligible level, P_m was averaged for 30 s before the NMR measurement.

The optical signal was also used to measure the AFP efficiency, i.e., the efficiency of the inversion of the polarization. Incomplete inversion of the magnetization results mainly from violations of the adiabatic condition that occur when ^{3}He atoms move through a magnetic field gradient. Consequently, the effect of a given gradient is much smaller for the water signal. The AFP efficiency ϵ is defined as

$$\epsilon \equiv \frac{P_0 - P_f}{2P_0} , \tag{15}$$

where P_0 and P_f are the polarizations before and after the sweep, respectively. Since ϵ is very close to unity ($\epsilon = 0.988$), we determined it by measuring P_f after eight sweeps in rapid succession. A small correction to the NMR data was applied because of the imperfect efficiency of adiabatic fast passage. To determine the correction to the NMR results we measured the dependence of the height of the ^{3}He and water signals on the measured AFP efficiency for ^{3}He. The AFP efficiency [Eq. (15)] was varied from $\epsilon = 0.92$ to 0.99 by applying a magnetic field gradient. Using empirical quadratic fits of the NMR signal height versus AFP efficiency, we found the reduction in $\mathcal{E}_0^h$ ($\mathcal{E}_0^p$) to be 0.4(0.1)% for our typical AFP efficiency. Based on these results, we corrected R [see Eq. (7)] by a factor of 1.003 ± 0.002.

We measured $\mathcal{E}_0^h$ from an unpolarized cell and found it to be consistent with zero within 0.2%. In addition, we checked whether the NMR signal varied linearly with the optical signal and whether there was an offset in this linear dependence. The offset was found to be

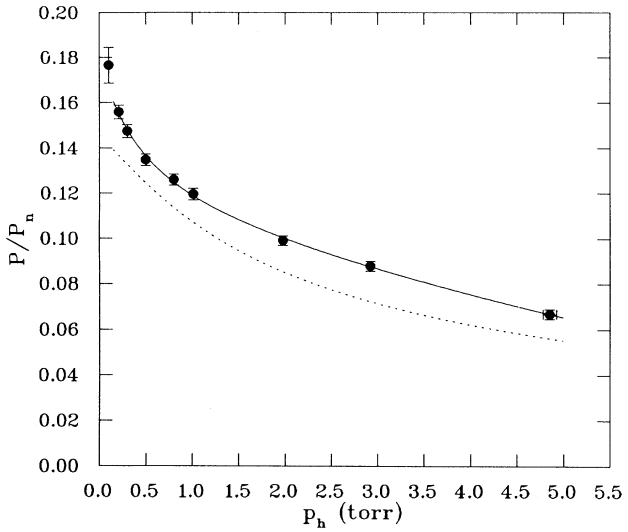

FIG. 7. The ratio of the degree of circular polarization of the 668-nm light to the nuclear polarization, P/P_n, vs p_h. The solid circles are measurements and the solid line is a fit for $p_h \geq 0.2$ torr using the procedure described in Sec. II C. The error bars displayed are the sum of the fit and systematic uncertainties added in quadrature. The dotted line is a fit of the data from Ref. [21].

$(0.2\pm0.2)\%$, where the uncertainty is dominated by the uncertainty in A_0.

C. Results

We have performed measurements at pressures ranging between 0.1 and 5 torr. Figure 7 shows our measurements of P/P_n vs p_h along with a fit of the data using the procedure described in Sec. II C. We included only the data for $p_h \geq 0.2$ torr in the fit. The data in Fig. 7 are also tabulated in Table I, where we have listed the inverse, P_n/P. For comparison, we have also listed the values obtained from a fit of the data in Ref. [21]. Our result at 0.5 torr is 7% below that of Ref. [21] and the difference increases to 13% at 0.2 torr and 18% at 3 torr.

Using $v_r = 2.03\times10^3$ m/s and $n = 3.22\times10^{22}$ atoms/m^3 (at 1 torr and 297 K), we obtain fit values of $\sigma_1 = (148\pm8)\times10^{-16}$ cm^2, $\sigma_2 = (198\pm290)\times10^{-16}$ cm^2, $\sigma_0 = (97\pm27)\times10^{-16}$ cm^2, and $Z = 0.748\pm0.073$. As was found in Ref. [21], the fit is insensitive to the value of the disalignment cross section σ_2.

TABLE I. Measurements of P_n/P as a function of p_h (for $T_h = 297$ K) and the results of a fit of these data using the procedure described in Sec. II C. We have also tabulated the results of a fit of the data in Ref. [21]. The fit and systematic uncertainties, discussed in the text, are also tabulated.

				Uncertainties	
p_h (torr)	P_n/P (data)	P_n/P (fit)	P_n/P[a] (fit)	Fit (%)	Systematic (%)
0.0998	5.67			0.5	4.5
0.207	6.42	6.44	7.3	0.4	1.9
0.299	6.78	6.75	7.5	0.4	1.9
0.499	7.42	7.33	8.0	0.3	1.9
0.800	7.94	8.02	8.7	0.3	1.9
1.010	8.37	8.43	9.3	0.3	2.1
1.977	10.09	9.97	11.6	0.3	2.1
2.92	11.38	11.42	13.8	0.3	2.5
4.85	14.98	14.98	17.8	0.3	3.1

[a]Reference [21].

D. Uncertainties

The uncertainties in our measurements are listed in Table I in two categories: fit uncertainty and systematic uncertainty. The fit uncertainty is the sum (in quadrature) of the typical uncertainties in the fitted values of $\mathcal{E}_0^p$ and $\mathcal{E}_0^h$. The total uncertainty is mainly systematic and the fit uncertainty is dominated by the $\pm0.3\%$ uncertainty in the fitted value of $\mathcal{E}_0^p$.

Table II lists the sources and magnitudes of the systematic uncertainties in our measurements. Let us first consider those uncertainties that can lead to day to day variations in measurements on a given ^{3}He cell. These include the uncertainty in the fitted value of $\mathcal{E}_0^h$ and a subset of the systematic uncertainties. This subset includes the uncertainties in quantities that are measured each day, namely, Q_h, K, and A_0. In addition, we must include the effect on the NMR signal of an error in locating the resonant frequency of the pickup coil (labeled C in Table II). The typical uncertainty in finding ω was $\pm0.05\%$, which leads to a $\pm0.4\%$ effect on the Lorentzian response of the pickup coil. The uncertainty assigned to K was the typical day to day variation of $\pm0.5\%$; the origin of this variation was not established, but is probably due to slight variations in the gain of the dc amplifier and positioning of the circular polarizer. The contribution of the uncertainty in A_0 generally increased with pressure because P/P_n decreases. The sum of all the uncertainties that cause day to day variations was found to be consistent with observed day to day variations in the measurements of P/P_n. The only exception to this statement was for the data acquired at 0.1 torr, where the variations in $\mathcal{E}_0^h$ were larger than expected. For 0.1 torr the systematic uncertainty listed in Table I is dominated by the standard deviation of our data set of 20 measurements.

Day to day variations in the measurements on a water

TABLE II. Contributions to the systematic uncertainty in P/P_n.

		Systematic errors		
Q_p, Q_h		0.7%	R	1.1%
K		0.5%	$\cos\theta$	0.3%
A_0	0.1–0.8 torr	0.3%	$M(B_0)$	0.5%
	1–3 torr	0.8%	Ellipticity	0.5%
	5 torr	2.0%	p_h (3,5 torr)	1.5%
C		0.4%	p_h (all others)	0.5%
T_p, T_h		0.2%	V_p, V_h	0.2%

cell originate from the uncertainty in the fitted value of $\mathcal{E}_0^p$ ($\pm 0.3\%$), the uncertainty in Q_p ($\pm 0.7\%$) and T_p ($\pm 0.2\%$), and the uncertainty C ($\pm 0.4\%$). The observed day to day variation in the measurements of $\mathcal{E}_0^p$ were consistent with the sum of these uncertainties added in quadrature. Several measurements of $\mathcal{E}_0^p$ were averaged to obtain a better value, but to be conservative, we did not reduce the magnitude of the uncertainties discussed above.

Systematic uncertainties that will not cause day to day variations are also listed in Table II. The uncertainty in the signal ratio R includes three contributions: the linearity of the electronics ($\pm 1\%$), the uncertainty in the small correction applied to R for imperfect adiabatic fast passage ($\pm 0.2\%$—see Sec. IV B), and the uncertainty in the water measurement due to nonlinearity in the ramp ($\pm 0.3\%$—see Sec. IV A). There is a small uncertainty of $\pm 0.3\%$ in the value of $\cos\theta$ and of $\pm 0.5\%$ in the magnetic field correction $M(B_0)$. Other sources of uncertainty have been discussed in the text: ellipticity (Sec. III C 2); p_h, V_p, and V_h (Sec. III B).

V. CONCLUSION

We have performed accurate NMR and optical measurements that calibrate an optical method for measuring nuclear polarization in ^{3}He. Specifically, we have measured the ratio of nuclear polarization in ^{3}He to the degree of circular polarization of the 668-nm light emitted from a polarized ^{3}He discharge. The range of these measurements is 0.1–5 torr and the typical uncertainty is $\pm 2\%$. We measure this ratio to be 7–18 % lower than the earlier results of Ref. [21], depending on the pressure.

ACKNOWLEDGMENTS

We gratefully acknowledge the help of Al Massey for designing and building the NMR electronics. We thank Robert Carr and Gabor Faludi for preparing many cells, and Jim Pendlay and Jack Richards for their technical support. We give special thanks for our interaction with Michele Leduc at L'Ecole Normale Supérieure and appreciate useful conversations with Kevin Lee, Cathleen Jones, and Laird Schearer. This work was supported by the National Science Foundation Grant Nos. PHY88-17296 and PHY91-15574.

APPENDIX A: CALIBRATION OF THE OPTICAL POLARIMETER

In this appendix we analyze the calibration of the optical polarimeter (see Fig. 3). We assume that the polarimeter is calibrated with an imperfect circular polarizer consisting of an ideal linear polarizer (L) followed by an imperfect quarter-wave plate (Q) (retardation $\phi_c \neq \pi/2$). The angle between the optic axis of the quarter-wave plate and the axis of the linear polarizer is $\pi/4$. Because $\phi_c \neq \pi/2$, such a circular polarizer produces elliptically polarized light. Using matrix techniques [32], we analyze the propagation of elliptically polarized light through the polarimeter and determine the signal produced at the photomultiplier tube. While we also assume that the rotating quarter-wave plate (R) is imperfect, the linear polarizers (L and A) are assumed to be ideal because at 668 nm dichroic polarizers yield 99.998% linearly polarized light [33].

The amplitude of the electric field of the elliptically polarized light exiting the circular polarizer can be written [34] in a basis of linearly polarized waves as

$$\mathbf{E}_c = a_1\hat{\mathbf{x}} + ia_2\hat{\mathbf{y}} \tag{A1}$$

or in a basis of circularly polarized waves as

$$\mathbf{E}_c = a_+(\hat{\mathbf{x}} + i\hat{\mathbf{y}}) + a_-(\hat{\mathbf{x}} - i\hat{\mathbf{y}}) \ . \tag{A2}$$

The degree of circular polarization of the light is given by

$$P_c \equiv \frac{a_+^2 - a_-^2}{a_+^2 + a_-^2} = \frac{2a_1a_2}{a_1^2 + a_2^2} \ , \tag{A3}$$

and the degree of linear polarization of the light is

$$P_l \equiv \frac{a_1^2 - a_2^2}{a_1^2 + a_2^2} \ . \tag{A4}$$

Note that $P_c^2 + P_l^2 = 1$. The matrix for the rotating quarter-wave plate is $Q' = \tilde{R}QR$, where

$$Q = \begin{bmatrix} \exp(-i\phi_r/2) & 0 \\ 0 & \exp(i\phi_r/2) \end{bmatrix} , \tag{A5}$$

and R is the rotation matrix, given by

$$R = \begin{bmatrix} \cos(\omega t) & \sin(\omega t) \\ -\sin(\omega t) & \cos(\omega t) \end{bmatrix} . \tag{A6}$$

ϕ_r is the retardation of the rotating quarter-wave plate and ω is the rotation frequency. Similarly, the matrix for the analyzing linear polarizer (A) is

$$L' = \tilde{R}LR = \begin{bmatrix} \cos^2\alpha & \cos\alpha\sin\alpha \\ \cos\alpha\sin\alpha & \sin^2\alpha \end{bmatrix} , \tag{A7}$$

where

$$L = \begin{bmatrix} 1 & 0 \\ 0 & 0 \end{bmatrix} , \tag{A8}$$

and ωt has been replaced by α, the angle between the axis of the linear polarizer and the $\hat{\mathbf{x}}$ axis. The electric field of the light at the photomultiplier tube is $\mathbf{E}_p = L'Q'\mathbf{E}_c$ and the intensity is proportional to E_p^2. Performing the matrix multiplication yields

$$\begin{aligned} E_p^2 = \tfrac{1}{2}\{ & 1 + P_c\sin\phi_r\sin(2\omega t - 2\alpha) \\ & + P_l[\cos^2(\phi_r/2)\cos(2\alpha) \\ & + \sin^2(\phi_r/2)\cos(4\omega t - 2\alpha)]\} \ , \end{aligned} \tag{A9}$$

where we have set $a_1^2 + a_2^2 = 1$ for normalization. For an ideal system, $P_c = 1$, $P_l = 0$, and $\phi_r = \pi/2$; under these conditions, E_p^2 shows only the expected oscillation at the frequency 2ω, with maximum amplitude. Elliptical polarization of the light exiting the circular polarizer ($P_l \neq 0$) introduces an oscillation at a frequency 4ω and a

dependence on the relative orientation of the two linear polarizers in the system, both proportional to P_l. (These effects can be understood by considering the limiting case of linearly polarized light exiting the circular polarizer.) Imperfect retardation in the rotating quarter-wave plate reduces the magnitude of the oscillation at 2ω and modifies the magnitude of the effects of ellipticity.

Since the lock-in amplifier only responds to the oscillation at the frequency 2ω, the degree of circular polarization measured by the polarimeter, P_m, is given by

$$P_m \equiv \frac{A}{D} = \frac{P_c \sin\phi_r}{1+P_l\cos^2(\phi_r/2)\cos(2\alpha)} , \tag{A10}$$

where A and D are the ac and dc components of E_p^2, respectively. [For this theoretical discussion, we have set $K=1$ and $A_0=0$ in Eq. (13).] The polarimeter only yields the true degree of circular polarization of the light, P_c, when $\phi_r=\pi/2$ and $\alpha=n\pi/4$, where n is an odd integer. Let us compare the effect of imperfect circular polarization ($P_l\neq 0$) and imperfect retardation in the rotating quarter-wave plate ($\phi_r\neq\pi/2$). For $\phi_r=\pi/2$, P_m reduces to

$$P_m = \frac{P_c}{1+\frac{1}{2}P_l\cos(2\alpha)} . \tag{A11}$$

For $P_c\approx 1$, P_m exhibits a periodic variation in α with an amplitude of $\frac{1}{2}P_l$. For $P_c=0.99$, $\frac{1}{2}P_l=0.07$, so a relatively small deviation from perfect circularly polarized light can have a noticeable effect on the calibration of the polarimeter. In addition, the error introduced cannot simply be included in K (Sec. III C) because the oscillation is a manifestation of the elliptical polarization, hence the response of the polarimeter will be different for circularly polarized light. In the case where $\phi_r\neq\pi/2$ and $P_c=1$, P_m reduces to $P_m=\sin\phi_r$. For $\phi_r\approx\pi/2$, P_m is insensitive to the exact value of ϕ_r and the reduction in P_m can be included in K.

If we express P_c and P_l in terms of the retardation ϕ_c of the quarter-wave plate in the circular polarizer, we can compare the sensitivity of P_m for a given retardation error in either waveplate. The electric field at the output of the circular polarizer is given by

$$\mathbf{E}_c = Q'L\mathbf{E} , \tag{A12}$$

where $\mathbf{E}$ is an arbitrary normalized electric field at the input of the circular polarizer and ωt is replaced by $\pi/4$. Evaluation of Eq. (A12) and use of Eqs. (A3) and (A4) yields $P_c=\sin\phi_c$ and $P_l=\cos\phi_c$. Hence Eq. (A10) can be rewritten as

$$P_m = \frac{\sin\phi_c\sin\phi_r}{1+\cos\phi_c\cos^2(\phi_r/2)\cos(2\alpha)} . \tag{A13}$$

While a retardation error of 0.14 rad in ϕ_r yields only a 1.0% change in P_m, an equal error in ϕ_c (corresponding to $P_c=0.99$) yields an oscillation in P_m with an amplitude of 7.0%. Hence the measured polarization P_m is much more sensitive to the quality of the quarter-wave plate in the circular polarizer than to the quality of the rotating quarter-wave plate.

APPENDIX B: DEPENDENCE OF THE OPTICAL SIGNAL ON OBSERVATION ANGLE

The degree of circular polarization of the 668-nm radiation is simple to evaluate for radiation propagating along the quantization axis because only radiation from $\Delta m=\pm 1$ transitions must be considered and this light is circularly polarized. However, for observation off the quantization axis, the evaluation is somewhat more complex because there also exists linearly polarized radiation from $\Delta m=0$ transitions and the radiation from $\Delta m=\pm 1$ transitions is elliptically polarized [35]. To calculate the degree of circular polarization of the radiation, we must express the electric fields of the light emitted from $\Delta m=-1$, 0, and $+1$ transitions in a basis of circularly polarized waves and sum the intensities for each helicity. In spherical coordinates with the quantization axis along $\hat{\mathbf{z}}$ the electric field of the radiation is proportional to $\hat{\boldsymbol{\theta}}\sin\theta$ for $\Delta m=0$ transitions and $\hat{\boldsymbol{\theta}}\cos\theta\pm i\hat{\boldsymbol{\phi}}$ for $\Delta m=\pm 1$ transitions. Thus in the notation of Appendix A for a basis of circularly polarized waves, the intensities of the two helicities are given by

$$a_+^2 = \frac{a}{4}(1+\cos\theta)^2+\frac{b}{4}(1-\cos\theta)^2+\frac{c}{2}\sin^2\theta , \tag{B1}$$

$$a_-^2 = \frac{a}{4}(1-\cos\theta)^2+\frac{b}{4}(1+\cos\theta)^2+\frac{c}{2}\sin^2\theta , \tag{B2}$$

where a, b, and c are the intensities of the emitted radiation from $\Delta m=+1$, -1, and 0 transitions, respectively. If we assume that there is no electronic alignment then $c=(a+b)/2$ and the degree of circular polarization P_c is

$$P_c = \frac{a-b}{a+b}\cos\theta . \tag{B3}$$

The electronic alignment is formally defined as $\langle 3J_z^2-J(J+1)\rangle$ [3] and corresponds to preferential population of sublevels m_J and $-m_J$ as compared to m_J' and $-m_J'$. The electronic orientation is defined by $\langle J_z\rangle$ and corresponds to preferential population of sublevel m_J as compared to $-m_J$. In zero magnetic field, the hyperfine interaction in the $3\,^1D_2$ state produces electronic orientation but no alignment [3]. For finite magnetic fields, there is a coupling of orientation and alignment. For the small 30-G field used in our measurements, this coupling can be neglected.

[1] L. D. Schearer and Padetha Tin, J. Appl. Phys. **68**, 943 (1990).
[2] F. Laloë, Ann. Phys. (Paris) **6**, 5 (1971).
[3] M. Pavlovic and F. Laloë, J. Phys. (Paris) **31**, 173 (1970).
[4] F. D. Colegrove, L. D. Schearer, and G. K. Walters, Phys. Rev. **132**, 2561 (1963).
[5] G. Tastevin, P. J. Nacher, and F. Laloë, in *Proceedings on the Conference on Spin Polarized Quantum Systems, Tori-*

no, June, 1988, edited by S. Stringari (World Scientific, Singapore, 1989).
[6] M. Leduc, J. Phys. (Paris) Colloq. **51**, C6-317 (1990).
[7] G. H. Rutherford *et al.*, Rev. Sci. Instrum. **61**, 1460 (1990).
[8] K. P. Coulter *et al.*, Nucl. Instrum. Methods A **288**, 463 (1990).
[9] R. G. Milner, R. D. McKeown, and C. E. Woodward, Nucl. Instrum. Methods A **274**, 56 (1989).
[10] C. L. Bohler *et al.*, J. Appl. Phys. **63**, 2497 (1988).
[11] Thomas R. Gentile and Robert D. McKeown, preceding paper, Phys. Rev. A **47**, 456 (1993).
[12] G. Eckert *et al.*, Nucl. Instrum. Methods A **320**, 53 (1992).
[13] C. Larat, Ph.D. thesis, L'Ecole Normale Superieure, Paris, France, 1991.
[14] B. Blankleider and R. M. Woloshyn, Phys. Rev. C **29**, 538 (1984).
[15] C. E. Woodward *et al.*, Phys. Rev. Lett. **65**, 698 (1990); Phys. Rev. C **44**, R571 (1991).
[16] M. Leduc, S. B. Crampton, P. J. Nacher, and F. Laloë, Nucl. Sci. Appl. **2**, 1 (1984).
[17] E. W. Otten, Prog. Part. Nucl. Phys. **24**, 103 (1990).
[18] R. S. Timsit *et al.*, Can. J. Phys. **49**, 508 (1971).
[19] K. Lee, J. F. J. Van Den Brand, O. Hansen, and R. G. Milner, Nucl. Instrum. Methods (to be published).
[20] Joseph Hamel *et al.*, Opt. Commun. **63**, 114 (1987).
[21] M. Pinard and J. Van Der Linde, Can. J. Phys. **52**, 1615 (1974).
[22] N. Bigelow, P. J. Nacher, and M. Leduc, J. Phys. (Paris) (to be published).
[23] F. Bloch, Phys. Rev. **70**, 460 (1946).
[24] A. Abragam, *The Principles of Nuclear Magnetism* (Oxford University Press, Oxford, England, 1961).
[25] M. Santini, Suppl. Nuovo Cimento XVI-X, 680 (1960).
[26] F. J. Low and H. E. Rorschach, Phys. Rev. **120**, 1111 (1960).
[27] D. Pines and C. P. Slichter, Phys. Rev. **100**, 1014 (1955).
[28] M. Pinard, Ph.D. thesis, Université de Paris, Paris, France, 1973.
[29] H. H. Bukow, G. Heine, and M. Reinke, J. Phys. B **10**, 2347 (1977).
[30] Robert L. Brooks, Vincent F. Streif, and H. Gordon Berry, Nucl. Instrum. Methods **202**, 113 (1982).
[31] Charles P. Poole, Jr. and Horacio A. Farach, *Relaxation in Magnetic Resonance* (Academic, New York, 1971), p. 74.
[32] E. Hecht and A. Zajac, *Optics* (Addison-Wesley, Reading, MA, 1974), pp. 266–271.
[33] Optics Guide 5 (Melles Griot 1990 Catalog, Irvine, CA) (unpublished). Also confirmed by direct measurement.
[34] J. D. Jackson, *Classical Electrodynamics* (Wiley, New York, 1975), pp. 273–278.
[35] E. U. Condon and G. H. Shortley, *The Theory of Atomic Spectra* (Cambridge University Press, Cambridge, England, 1976), pp. 90–93.